



Space Weather

RESEARCH ARTICLE

10.1029/2020SW002525

Key Points:

- First report on storm-time modeling of TEC across the entire African region is presented
- Inclusion of time history of geomagnetic activity indicators improved TEC modeling by about 5% and 12% in middle and low latitudes, respectively
- Result of calibration of COSMIC-TEC to GPS-TEC equivalent is demonstrated

Correspondence to:

D. Okoh,
okodan2003@gmail.com

Citation:

Okoh, D., Habarulema, J. B., Rabiu, B., Seemala, G., Wisdom, J. B., Olwendo, J., et al. (2020). Storm-time modeling of the African regional ionospheric total electron content using artificial neural networks. *Space Weather*, 18, e2020SW002525. <https://doi.org/10.1029/2020SW002525>

Received 20 APR 2020

Accepted 7 AUG 2020

Accepted article online 10 AUG 2020

Storm-Time Modeling of the African Regional Ionospheric Total Electron Content Using Artificial Neural Networks

Daniel Okoh^{1,2,3} , **John Bosco Habarulema**^{2,4} , **Babatunde Rabiu**^{1,3} , **Gopi Seemala**⁵, **Joshua Benjamin Wisdom**⁶ , **Joseph Olwendo**⁷ , **Olivier Obrou**⁸, and **Tshimangadzo Merline Matamba**² 

¹Center for Atmospheric Research, National Space Research and Development Agency, Anyigba, Nigeria, ²Space Science, South African National Space Agency, Hermanus, South Africa, ³Institute for Space Science and Engineering, African University of Science and Technology, Abuja, Nigeria, ⁴Department of Physics and Electronics, Rhodes University, Grahamstown, South Africa, ⁵Indian Institute of Geomagnetism, Navi Mumbai, India, ⁶Department of Physics, Kebbi State University of Science and Technology, Aliero, Nigeria, ⁷Department of Physics, Pwani University, Kilifi, Kenya, ⁸Laboratoire de Physique de l'Atmosphère, Université de Cocody, Abidjan, Côte d'Ivoire

Abstract This paper presents the development of a storm-time total electron content (TEC) model over the African sector for the first time. The storm criterion used was $|Dst| \geq 50$ nT and $K_p \geq 4$. We have utilized Global Positioning System (GPS) observations from 2000 to 2018 from about 252 receivers over the African continent and surroundings within spatial coverage of 40°S–40°N latitude and 25°W–60°E longitude. To increase data coverage in areas devoid of ground-based instrumentation including oceans, we used the available radio occultation Constellation Observing System for Meteorology, Ionosphere, and Climate (COSMIC) TEC from 2008 to 2018. The model is based on artificial neural networks which are used to learn the relationship between TEC and the corresponding physical/geophysical input parameters representing factors which influence ionospheric variability. An important result from this effort was the inclusion of the time history of the geomagnetic activity indicators $\left(\frac{dK_p}{dt} \text{ and } \frac{dDst}{dt}\right)$ which improved TEC modeling by about 5% and 12% in middle and low latitudes, respectively. Overall, the model performs comparatively well with, and sometimes better than, the earlier single station modeling efforts even during quiet conditions. Given that this is a storm-time model, this result is encouraging since it is challenging to model ionospheric parameters during geomagnetically disturbed conditions. Statistically, the average root-mean-square error (RMSE) between modeled and GPS TEC is 5.5 TECU (percentage error = 30.3%) and 5.0 TECU (percentage error = 30.4%) for the Southern and Northern Hemisphere midlatitudes respectively compared to 7.5 TECU (percentage error = 22.0%) in low latitudes.

1. Introduction

Geomagnetic storms are momentary disturbances of the Earth's magnetic field as a result of energy transferred to the magnetosphere from the solar wind. The solar wind is an outflow of plasma from the Sun, consisting of charged particles with typical kinetic energies of the order of a few kilo-electronvolts. When solar winds hit the Earth's magnetosphere, they generate shock waves and interactions that manifest as geomagnetic storms. Geomagnetic storms affect several aspects of space weather, including the ionosphere. For a relatively long time, a lot of research has been devoted to understanding how geomagnetic storms affect the ionosphere (e.g., Appleton, 1950; Findlay et al., 1969; Nava et al., 2016; Sato, 1957; Yeh et al., 1994; and many others). A compilation of results from these studies show that geomagnetic storms can lead to remarkable increases in the ionospheric ionization levels referred to as positive ionospheric storms (e.g., Namgaladze et al., 2000; Ngwira et al., 2012; Pedatella et al., 2009), remarkable decreases in the ionospheric ionization levels referred to as negative ionospheric storms (e.g., Mikhailov & Schlegel, 1998; Strickland et al., 2001; Yue et al., 2016), or insignificant changes in the ionospheric ionization levels referred to as non-significant ionospheric storms (e.g., Adekoya et al., 2012; Matamba et al., 2015; Uwamahoro & Habarulema, 2015).

©2020. The Authors.

This is an open access article under the terms of the Creative Commons Attribution License, which permits use, distribution and reproduction in any medium, provided the original work is properly cited.

In Africa, a good number of research have also been conducted to investigate ionospheric variation during geomagnetic storms (e.g., Adebesin, 2008; Adebiyi et al., 2014; Habarulema, 2010; Joshua et al., 2018; Matamba & Habarulema, 2018; Olawepo & Adeniyi, 2012; Rabiu et al., 2007; Uwamahoro et al., 2018; and many more).

Ionospheric storms have remained a contemporary research interest because of the growing concern to improve modeling accuracy of ionospheric behavior during geomagnetic storms. In recent times, the major challenge has been to accurately model quantitative deviations in ionospheric parameters, like total electron content (TEC), during geomagnetic storms. This challenge is made even more complicated by indications from previous research (e.g., Joshua et al., 2018; Uwamahoro et al., 2018) that there may not be a direct relationship between magnitudes of the deviations and the storm intensities. The deviations have also been convincingly demonstrated to exhibit spatial variations that depend on location.

The first regional TEC model over the entire African region (AfriTEC) was developed by applying the method of neural networks on empirical observations obtained from ground-based Global Positioning System (GPS) receivers and from GPS receivers on board the Constellation Observing System for Meteorology, Ionosphere, and Climate (COSMIC) mission (Okoh et al., 2019). This was a quiet-time-based model; only quiet-time observations ($-20 \text{ nT} \leq Dst \leq 20 \text{ nT}$) were used. In the present work, a version of the storm-time model for the AfriTEC is developed by using artificial neural networks to model TEC measurements obtained across Africa during storm periods ($|Dst| \geq 50 \text{ nT}$ and $Kp \geq 4$). Using data for all (both quiet and storm) periods does allow the networks to learn storm-time variations, so long as storm indices are included as inputs (e.g., Habarulema, 2010; Okoh et al., 2016). However, Okoh et al. (2019) observed that including data from all periods does not allow the networks to adequately learn responses to TEC during storm conditions. This was explained to be due to obvious reason that vast majority of data for all periods are quiet-time data, and so patterns for quiet-time are predominantly “seen” by the neurons. This prompted the idea used in the present work, which is to increase proportion of the storm-time data, thereby improving concentration of the neurons on storm-time variations and so better performance of the model for the storm periods. Previous efforts of storm-time modeling over the African sector were largely restricted to single or more station models but did not encompass the whole African region due to limited observations. This is the first report of storm-time TEC modeling across the entire African region. The model is developed for operational purposes and has been proposed for real-time TEC monitoring at the Space Weather Center of the South African National Space Agency, Space Science.

2. Data

Data used in this work include GPS data (obtained from both ground-based and COSMIC satellite-borne GPS receivers) and indices for solar and geomagnetic activities. These data sets are explained next.

2.1. Ground-Based GPS Data

Ground-based GPS data were obtained from a total of 252 GPS receiver stations in different locations of the African region as shown by the red dots in Figure 1. The data included all available data from the stations for years 2000–2018, during geomagnetic storm periods. The criteria for geomagnetic storm selection were $|Dst| \geq 50 \text{ nT}$ and $Kp \geq 4$.

Data were obtained in Receiver Independent Exchange (RINEX) format from the following sources: the African Geodetic Reference Frame (AFREF), the South African network of continuously operating GNSS base stations (TRIGNET), the University of California, San Diego, SOPAC, and CSRC GARNER GPS Archive, the National Aeronautics and Space Administration's Crustal Dynamics Data Information System (CDDIS) Archive of GNSS products, the Global Data Center of the International GNSS Service, the UNAVCO Archive of GNSS Data, and the Geodetic Data Archiving Facility. RINEX data obtained from these sources were processed into TEC data using the GPS-TEC program (Rama Rao et al., 2006; Seemala & Valladares, 2011), which has been severally used and validated in many research papers (e.g., Akala et al., 2015; Catherine et al., 2017; Guyer & Can, 2013; Okoh et al., 2018; Olwendo et al., 2012; Panda et al., 2015; Rabiu et al., 2014; Uwamahoro et al., 2018). TEC data obtained from observations in which satellite elevation angles were less than or equal to 30° , were removed, in order to minimize multipath errors.

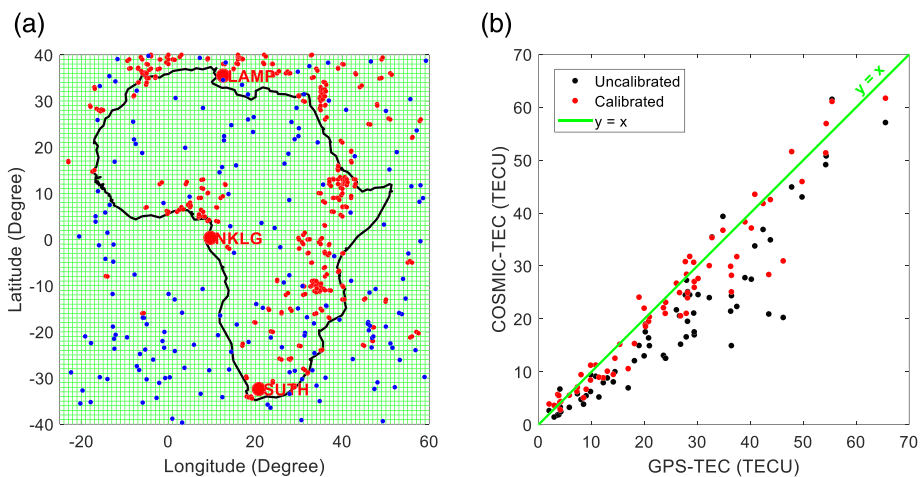


Figure 1. (a) African map showing locations of GPS receivers used (in red dots), and the coverage of the COSMIC-TEC during the storm period from 7 to 9 March 2012 (in blue dots). The blue dots are locations of maximum electron densities in various radio occultation (RO) events. The three labeled locations indicate GPS receiver stations from which data was used for testing of the model developed. The green mesh indicates $1^\circ \times 1^\circ$ grid cells into which the TEC observations were binned prior to the neural network training. (b) An illustration of how the calibrated and uncalibrated COSMIC-TECs compare with ground GPS-TEC at the $1^\circ \times 1^\circ$ grid cell of NKLG station.

TEC derived during radio occultation (RO) events, from the COSMIC mission (Chen-Joe, 2008; Syndergaard et al., 2006) were also used. The motivation for incorporating data from the COSMIC mission is based on the idea that the mission provides better spatial coverage across the region than the ground-based receivers. For our current study, COSMIC observations provide the much needed coverage over the Northern Hemispheric part of the African sector which has limited ground-based instrumentation, and oceanic areas. In Figure 1, coverage of ground-based GPS receivers is shown in red dots, while coverage of the COSMIC observations (for only 7–9 March 2012) is shown in blue dots. The figure shows that the COSMIC mission provided observations for locations (like the Sahara desert and the Atlantic Ocean) where there is sparse or no distribution of ground GPS receivers.

Second level COSMIC data (in “ionprf” format) were obtained from the COSMIC Data Analysis and Archive Centre. The data set comprises ionospheric electron density profiles for various RO events recorded in the African region (25°W – 60°E and 40°N – 40°S), and during the period from years 2008–2018. TEC was obtained from the COSMIC electron density profiles by integrating the electron densities for discrete RO events. The TEC obtained for a given RO event was assigned to the location with the maximum electron density. The profile for a given RO event can span a very wide area. The TEC value assigned to a particular location may therefore be contaminated by electron densities measured at other locations. To minimize errors that may result from these situations, only profiles in which the electron densities span less than 10° in latitude and less than 15° in longitude were integrated to derive TEC used in this work. Also, only data set satisfying the storm criteria ($|Dst| \geq 50$ nT and $K_p \geq 4$) was used.

Another consideration is that there is disparity between TECs derived from COSMIC and those derived from ground GPS receivers. For instance, the upper integration limits for TEC are respectively ~ 800 and $\sim 20,200$ km for the COSMIC-TEC and the ground GPS-TEC. To account for this disparity, we calibrated the COSMIC-TEC to obtain corresponding ground GPS-TEC using the method described by Okoh et al. (2019). The method basically involves using neural networks to learn the relationship between the two data sets for periods and locations for which there are available data from the two sources. The trained network is then used to scale the COSMIC values to corresponding ground-based GPS values. Figure 1b is an illustration of how the calibrated and uncalibrated COSMIC-TECs compare with the GPS measurements obtained at the $1^\circ \times 1^\circ$ grid cell of NKLG station. The green line (labeled $y = x$) is the identity line (having unit slope and zero intercept). It is the locus of ideal points in which the COSMIC-TEC is exactly equal to the GPS-TEC. The points closer to the line therefore present better agreement between the COSMIC-TEC and the GPS-TEC. Figure 1b clearly indicates that the calibrated COSMIC-TECs (red dots) are generally closer to the identity line than the corresponding uncalibrated COSMIC-TECs (black dots). The uncalibrated

COSMIC-TEC values typically fall below the identity line, indicating that they are smaller than corresponding GPS-TEC values. This shortfall is expected since the upper integration limit for the COSMIC-TEC is less than that of the GPS-TEC. The reason for engaging the calibration procedure is evident in Figure 1b. The figure clearly indicates that the calibration procedure was effectively used to tune the COSMIC-TEC values closer to corresponding GPS-TEC values.

TECs derived from both COSMIC and ground-based GPS receivers were then pooled together, and binned in hourly grids of $1^\circ \times 1^\circ$ cells as illustrated in Figure 1. It is these hourly values that were used for the neural network training described in section 3.

3. Methods

The method of artificial neural networks was used to model TEC variations during geomagnetic storm periods over the African region. The Bayesian regularization backpropagation algorithm (Bayes, 1763; Burden & Winkler, 2008; Laplace, 1812; MacKay, 1992) was used for training of the networks, and implementation was done using MATLAB's trainbr function and other functions in MATLAB's neural network toolbox.

3.1. Data Splitting and Normalization

Prior to training, the data set was split in three portions: for training, validation, and testing. The test data set was first formulated. It was constituted from the following two sets of data:

1. All data from each of the $1^\circ \times 1^\circ$ grid cells containing the three stations of LAMP (geographic: 12.6°E , 35.5°N ; geomagnetic: 26.6°N), NKLG (geographic: 9.7°E , 0.4°N ; geomagnetic: 8.0°S), and SUTH (geographic: 20.8°E , 32.4°S ; geomagnetic: 41.1°S), as shown in Figure 1. The three stations were chosen such that they respectively represent stations in the midlatitude (Northern Hemisphere) region, equatorial region, and midlatitude (Southern Hemisphere) region. They were also chosen such that they are separated by not more than 1 hr in longitude so that TEC profiles from the stations are not significantly separated in time. Finally, the stations were selected because they each had significant amount of data during the storm periods. These represented 5.58% of the entire data set.
2. All data sets recorded in year 2012, a year of moderate solar activity. These represented 9.55% of the entire data set.

The test data set described in (i) and (ii) which represented 15.13% of the entire data set formed the unseen data used for the final testing/verification of the model performance. The validation data set was formulated to comprise all data recorded during year 2015 (a year of high solar activity) and year 2008 (a year of low solar activity). This data set was utilized for deciding/choosing the best network from the several groups of networks trained during this study. Put together, the validation data set represented 14.69% of the entire data set. The remaining 70.18% of the entire data set was used for training or simply model development.

The training data was normalized using MATLAB's "mapminmax" processing function. The "tansig" function (which implements the hyperbolic tangent) was used as the transfer function between the input layer and the hidden layer, as well as between the hidden and the output layer.

3.2. Neural Network Inputs and Validation

The first stage of the modeling involved deciding the inputs that will facilitate the network's learning of TEC behavior during storm conditions. We started off with the base input layer neurons representing input parameters that were used in Okoh et al. (2019) for quiet-time modeling. The standard factors influencing TEC variability are seasonal variation represented by day number of the year (DOY), diurnal variation taken care of by the hour of the day (HH), spatial consideration (latitude and longitude) and solar activity ($F10.7$). Therefore, the base inputs included DOYs (sine component of the day of year), DOYc (cosine component of the day of year), HHs (sine component of the local time), HHc (cosine component of the local time), longitude, latitude, and $F10.7$. At least, an additional input layer neuron is required to facilitate the network's learning of TEC behavior during storm conditions. There was an option to include the Dst index or K_p index or both indices. To make an informed choice, we first trained three different sets of networks. For the first set, we included the Dst as an additional input layer neuron to the base input layer neurons described above. For the second set, we included the K_p as an additional input layer neuron to the base input layer neurons. And for the third set, we included both Dst and K_p as additional input layer neurons to the base input layer.

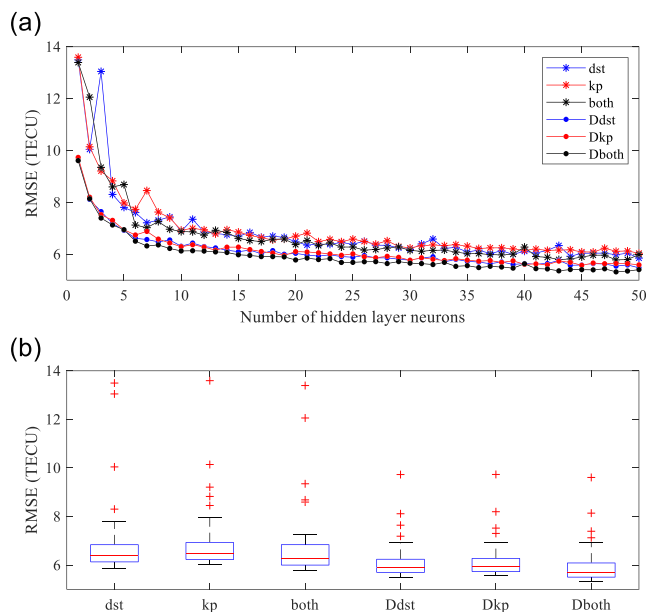


Figure 2. (a) RMSEs of six different sets of networks trained to test veracity of the storm index inputs. (b) Box and whisker plot showing distributions of the RMSEs.

supported our inclusion of both indices (rather than one of them) as inputs for our final network.

Considering that the effects of geomagnetic storms on TEC response could also be delayed, we furthermore investigated the behavior of the networks when provided with history of the storm indices as additional input layer neurons. This consideration is based on previous reports (e.g., Dubazane & Habarulema, 2018; Scherliess & Fejer, 1999; Yamazaki & Kosch, 2015) which indicate that the equatorial electric field during active geomagnetic conditions depend on the history and present geomagnetic activity levels. We provided history of the storm indices as first-order time derivatives of the storm indices, computed as described in Equation 1.

$$\frac{dx}{dt} = \frac{x|_{t+\Delta t} - x|_t}{\Delta t} \quad (1)$$

where x is the storm index and Δt is 1 hr for the Dst index and 3 hr for the Kp index.

Again, we trained three additional sets of networks in which we included derivatives of the storm indices as input layer neurons to the network which already had both Dst and Kp included. For the first set, we included derivative of the Dst . For the second set, we included derivative of the Kp , and for the third set, we included derivatives of both Dst and Kp . As before, we trained a total of 50 neural networks for each case (varying the number of hidden layer neurons from 1 to 50). Each of the trained neural networks was used to predict the TEC values for the validation data set. And RMSEs were computed for the predictions, by taking the corresponding measured TEC values as reference. Results of the RMSEs are also shown in Figure 2. In the legend of Figure 2a, “Ddst” represents RMSEs for the network which has derivative of Dst included, “Dkp” represents values for the network with derivative of Kp included, and “Dboth” represents the network with derivatives of both Dst and Kp included.

Again, Figure 2a clearly shows that the network which has derivative of both Dst and Kp included as inputs performs better than the networks which have either of the derivatives included. This is indicated by the observation that the RMSEs were, very often, lower for the network which has derivatives of both indices included. This is clearly corroborated by the box and whisker plot of Figure 2b, where the median of the error distribution is least for the network which has derivatives of both indices included. This is the set of network that was finally used for our storm model. In particular, we adopted the network which has 48 hidden layer neurons, because it gave the least error (RMSE = 5.3 TECU;

neurons. A total of 50 neural networks were trained in each case (varying the number of hidden layer neurons from 1 to 50). Each of the trained neural networks was then used to predict the TEC values for the validation data set. Regarding the corresponding measured TEC values as reference, the root-mean-square errors (RMSEs) for the neural network predictions were computed.

Figure 2a shows how the computed RMSEs compare with each other. In the figure legend, “dst” represents RMSEs for the network which has Dst included to the base input layer neurons, “kp” represents values for the network with Kp included, and “both” represents the network with both Dst and Kp included. Although the differences are small, Figure 2a clearly shows that the network which has both Dst and Kp included as inputs performs better than the networks which have either of the indices included. This is indicated by the observation that the RMSEs were, very often, lower for the network which has both indices included. Statistics of the errors are shown in the box and whisker plot of Figure 2b. On each box, the central mark indicates the median, and the bottom and top edges of the box indicate the 25th and 75th percentiles, respectively. The whiskers extend to the most extreme data points not considered outliers, and the outliers are plotted individually using the “+” symbol (Mathworks, 2020). The median (central marks in the boxes) is lower for the network which has both Dst and Kp included. This shows that, in general, the errors are smaller for this network and this further supports our inclusion of both indices (rather than one of them) as inputs for our final network.

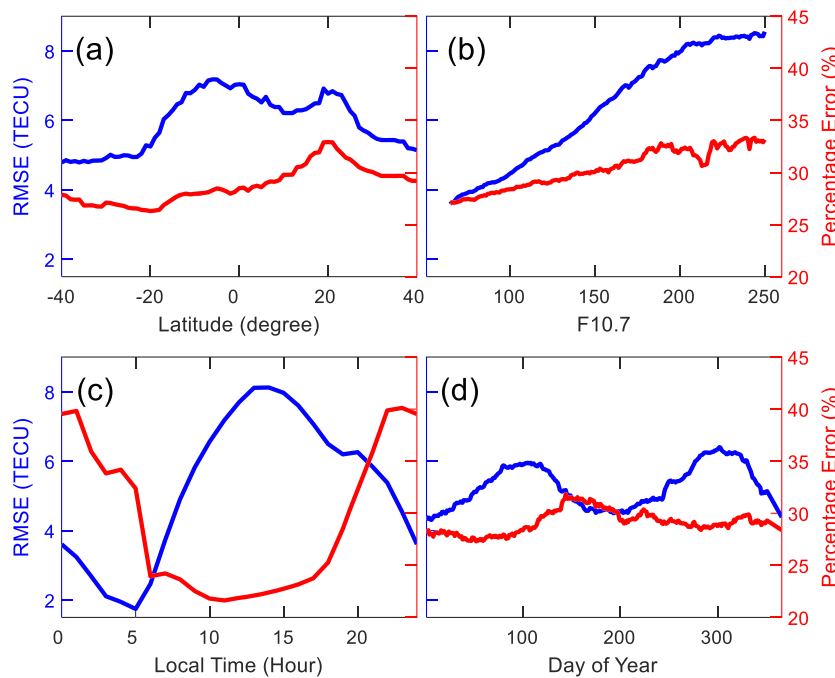


Figure 3. Variations of the RMSEs and percentage errors on the test data set under conditions of varying (a) latitudes, (b) F10.7 values, (c) local times, and (d) days of the years.

percentage error = 27.4%) on the validation data set. Percentage error is computed using the formula in Equation 2.

$$\text{Percentage error} = \frac{1}{n} \sum_{i=1}^n \frac{|\text{Observed TEC}_i - \text{Modeled TEC}_i|}{\text{Observed TEC}_i} \times 100 \quad (2)$$

where n is the number of observations used in computation of the percentage error.

The worst performing network in the figure has one hidden layer neuron; the RMSE is 13.7 TECU, and the percentage error is 74.6%, which is almost three times that of the best performing network. The adopted network is implemented as a MATLAB function that is included in the Appendix A of this paper. Figures 4–7 further demonstrate that this same set of network (having both derivatives of Dst and Kp included as input layer neurons) performs better on the test data set, in terms of minimizing the prediction errors, than the set of networks having either derivatives of Dst or Kp included. Interestingly, Figure 2a reveals that there is a relatively wide gap between the RMSEs of the set with and without the derivatives included. This is an indication that the derivatives are significant inputs for storm-time TEC modeling.

3.3. Error Analysis

Error analysis was conducted, on the test data set, to provide information on the magnitude of errors expected in using the final neural network model developed. Figures 3a–3d represent errors obtained in using the neural network model to make predictions of the test data set for varying conditions. In Figure 3a, the RMSEs were computed over different latitudes. The figure indicates that the RMSEs are larger around the equatorial region (about 7 TECU), and they decrease toward the midlatitude regions (about 5 TECU). Interestingly, the error plot contains signature of the equatorial ionization anomaly, in which a double peak is built around the magnetic equator.

Figure 3b indicates that the RMSEs are larger during periods of high solar activity (about 8 TECU for $F10.7 > 200$), and they decrease during periods of low solar activity (about 4 TECU for $F10.7 < 100$). Figure 3c shows diurnal variation of the RMSEs. The figure shows that the RMSEs are larger during local daytimes (about 8 TECU at 14:00 LT), and they decrease during local nighttimes (about 2 TECU at 05:00 LT). Figure 3d shows the seasonal variation of the RMSEs. The RMSEs are larger during equinoxes (about

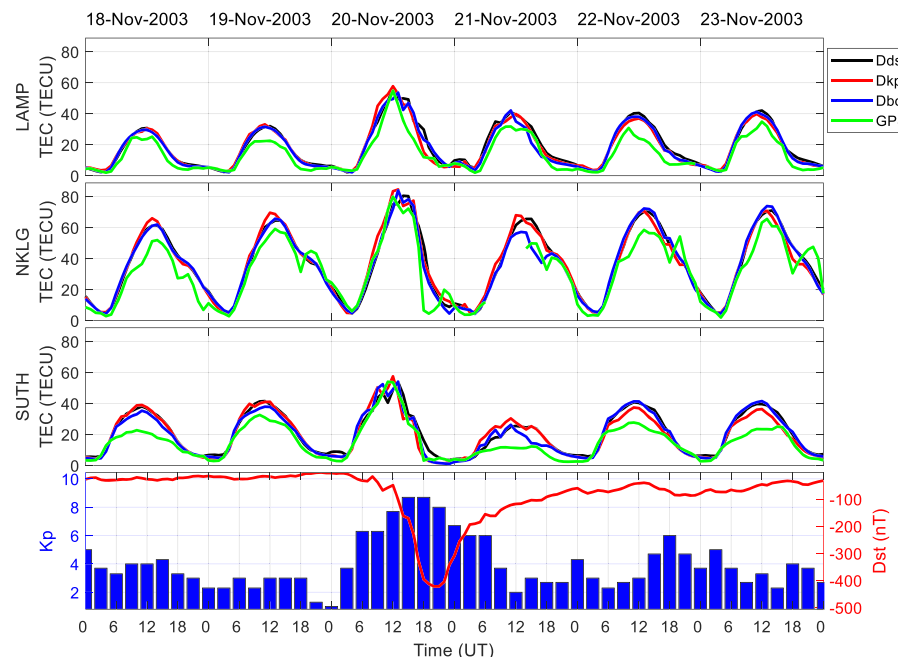


Figure 4. Modeled TECs versus GPS TECs at LAMP, NKLG, and SUTH, during the storm of 20 November 2003. The green plots represent TEC data from the GPS receivers. The black, red, and blue plots respectively represent TECs predicted from the models that include derivatives of Dst , derivatives of K_p , and derivatives of both Dst and K_p indices.

6 TECU), and they decrease during solstices (about 4.5 TECU). The error plots in Figure 3 point to the reality that the errors are larger when the TEC magnitudes are correspondingly larger, and vice versa. The larger error values obtained in the equatorial region is also potentially linked to the difficulty associated with modeling the region due to large TEC gradients and peculiar phenomena like the equatorial anomaly (Hunt et al., 2000; Okoh et al., 2018; Uwamahoro et al., 2019).

It is important to interpret behavior of the percentage error plots, especially in Figure 3c where it appears that the RMSE and percentage error are inversely related. This is not a case of inverse relation between the RMSE and percentage error. Rather, the percentage error (see Equation 2) is similar to a ratio of the error and the observed TEC. The implication is that the value of the percentage error decreases with increasing value of observed TEC, provided that the error is “fairly” constant, or not changing, in proportion, as much as the observed TEC does. There are notable variations of observed TECs in diurnal profiles; the observed TECs change much more rapidly than the errors do, especially during the ascending and descending phases of the diurnal profile. The result is that the percentage error decreases as the observed TEC increases and vice versa, leading to the scenario seen in Figure 3c. A similar explanation also applies to the observations that are noted in the rest of Figure 3.

In general, the developed model demonstrates performance that is comparable to, and mostly better than, other existing ones in the region, in terms of minimizing the prediction errors. We obtained an RMSE of 5.8 TECU (percentage error = 25.7%) when computed over our entire test data set. Habarulema et al. (2007) reported an average RMSE of 8.5 TECU for a neural network-based model developed over the South African region. Okoh et al. (2016) reported average RMSE values that are typically between 6.0 and 8.5 TECU for a neural network-based model developed over Nigeria. Interestingly, a very recent single-station study in the region (Habyarimana et al., 2020) reported an RMSE of 5.7 TECU which is very similar to the 5.8 TECU value obtained in the present study. The present study however exhibits two advantages. First, it is a wide-region model, and so it is expected to be less accurate than a single-station model. The comparable accuracy obtained is therefore an advantage. Second, the model developed in the present study is a storm-time model. Ionospheric variations during geomagnetic storm conditions are usually more erratic than during geomagnetically quiet conditions. It is therefore expected that quiet-time models should have better accuracy when compared to storm-time models. The comparable accuracy demonstrated by the model is therefore a

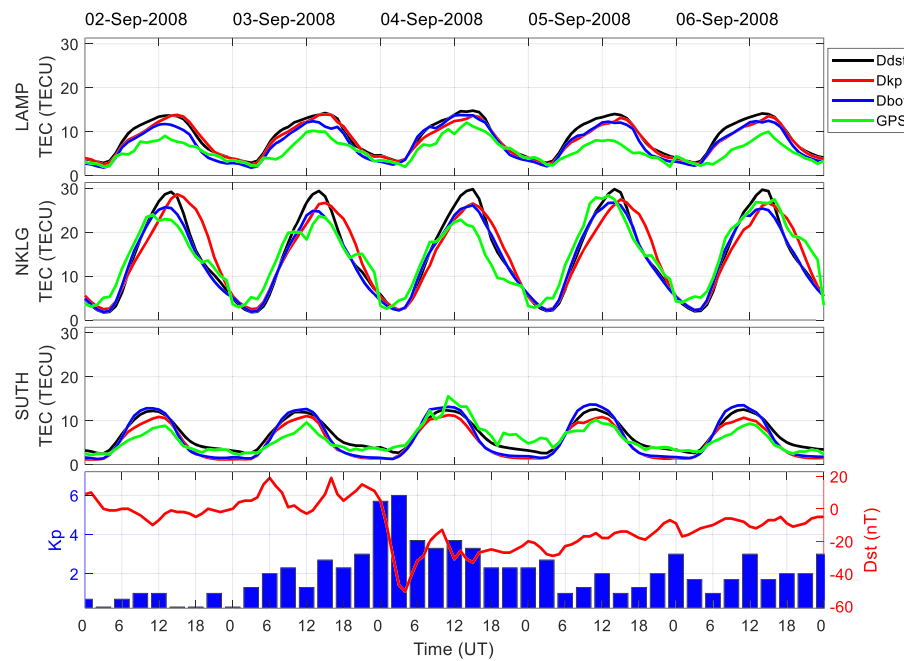


Figure 5. Modeled TECs versus GPS TECs at LAMP, NKLG, and SUTH, during the storm of 4 September 2008. The green plots represent TEC data from the GPS receivers. The black, red, and blue plots respectively represent TECs predicted from the models that include derivatives of Dst , derivatives of Kp , and derivatives of both Dst and Kp indices.

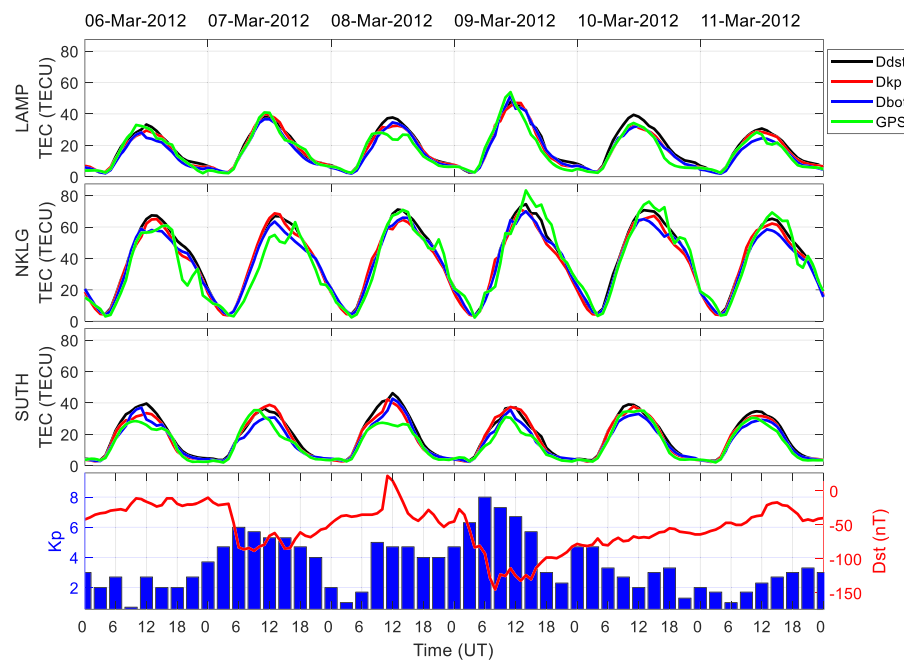


Figure 6. Modeled TECs versus GPS TECs at LAMP, NKLG, and SUTH, during the storms of 7 and 9 March 2012. The green plots represent TEC data from the GPS receivers. The black, red, and blue plots respectively represent TECs predicted from the models that include derivatives of Dst , derivatives of Kp , and derivatives of both Dst and Kp indices.

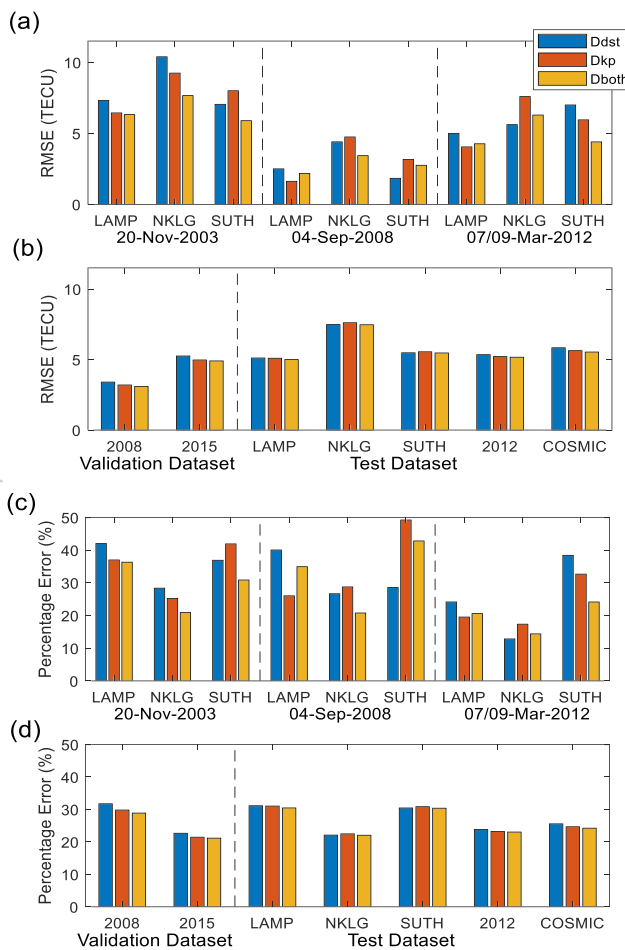


Figure 7. Bar chart of RMSEs computed for (a) the stations of LAMP, NKLG, and SUTH, during the storm periods of 20 November 2003, 4 September 2008, and 7/9 March 2012, (b) the validation and test data sets used. Bar chart of percentage errors computed for (c) the stations of LAMP, NKLG, and SUTH, during the storm periods of 20 November 2003, 4 September 2008, and 7/9 March 2012, (d) the validation and test data sets used.

the northern midlatitude station of LAMP. There was also slight increase in GPS-TEC during the intense storm of 9 March 2012 for the equatorial station of NKLG, and this was captured by the models. In overall, the model TEC profiles were close to the GPS-TEC profiles and interestingly captured the changes observed in GPS-TEC during the storm periods.

The model with both Dst and Kp derivatives included as inputs was more consistent in predicting TEC values that are close to the GPS-TEC values. Using the GPS-TEC values as reference, RMSEs were computed for the three models. Results of the RMSE values for the three models, computed for the illustrated storm periods (Figures 4–6), are shown in the bar chart of Figure 7a. Figure 7b shows information on the RMSE values for the three models, computed for all groups of the validation and test data sets. RMSE values for the validation data set (in Figure 7b) show that the model with both Dst and Kp derivatives as inputs gave the least errors when compared to the models with either the Dst derivatives or the Kp derivatives as inputs. The model with both Dst and Kp derivatives as inputs was therefore adopted, in this work, as the best model. This result is further corroborated by RMSEs computed using the test data sets.

To evaluate the effect of introducing the Dst and Kp derivatives, we compare RMSEs obtained from the network which includes the derivatives, against RMSEs obtained from the network which does not include the

benefit. What distinguishes this model from the previous studies is the inclusion of the history ($\frac{dKp}{dt}$ and $\frac{dDst}{dt}$) as additional inputs to take into account the delayed TEC response to the geomagnetic storms.

4. Results and Discussion

Figures 4–6 represent plots of the GPS-TEC and predicted TECs using the models with storm index derivatives included as input. The storms illustrated in Figures 4–6 are respectively the storms of 20 November 2003, 4 September 2008, and 7/9 March 2012. The figures also include TEC plots for about 2 days before and after the storm main phases. The illustrated storms were chosen such that they cover storm events of different magnitudes, occurring during different solar activity periods, and occurring during different seasons. The storm of 20 November 2003 (illustrated in Figure 4) was a super storm (minimum $Dst = -422$, maximum $Kp = 8.7$). The storm period was during a high solar activity period ($F10.7 \sim 170$) and in the December solstice season. The storm of 4 September 2008 (illustrated in Figure 5) was a moderate storm (minimum $Dst = -51$, maximum $Kp = 6$). The storm occurred during a period of low solar activity ($F10.7 \sim 67$) and in the September equinox season. Figure 6 illustrates two successive storms: the first is a moderate storm (minimum $Dst = -88$, maximum $Kp = 6$) which occurred on 7 March 2012, while the second is an intense storm (minimum $Dst = -145$, maximum $Kp = 8$) which occurred on 9 March 2012. The storms occurred during a period of moderate solar activity ($F10.7 \sim 140$) and in the March equinox season.

The figures show that the neural network models correctly captured variations of TEC during most of the storm periods. The increase of GPS-TEC during the storm period of 20 November 2003 was correctly captured by the models in the three stations illustrated. For the moderate storm of 4 September 2008, Figure 5 shows that insignificant changes in the GPS-TEC values were recorded, except for the southern midlatitude station of SUTH, where very slight GPS-TEC increase was recorded during the storm day. The neural network models mostly captured these insignificant changes. Interestingly, the models also accurately captured the slight increase of TEC values during the storm periods of Figure 6 for LAMP. There was also slight increase in GPS-TEC during the intense storm of 9 March 2012 for the equatorial station of NKLG, and this was captured by the models. In overall, the model TEC profiles were close to the GPS-TEC profiles and interestingly captured the changes observed in GPS-TEC during the storm periods.

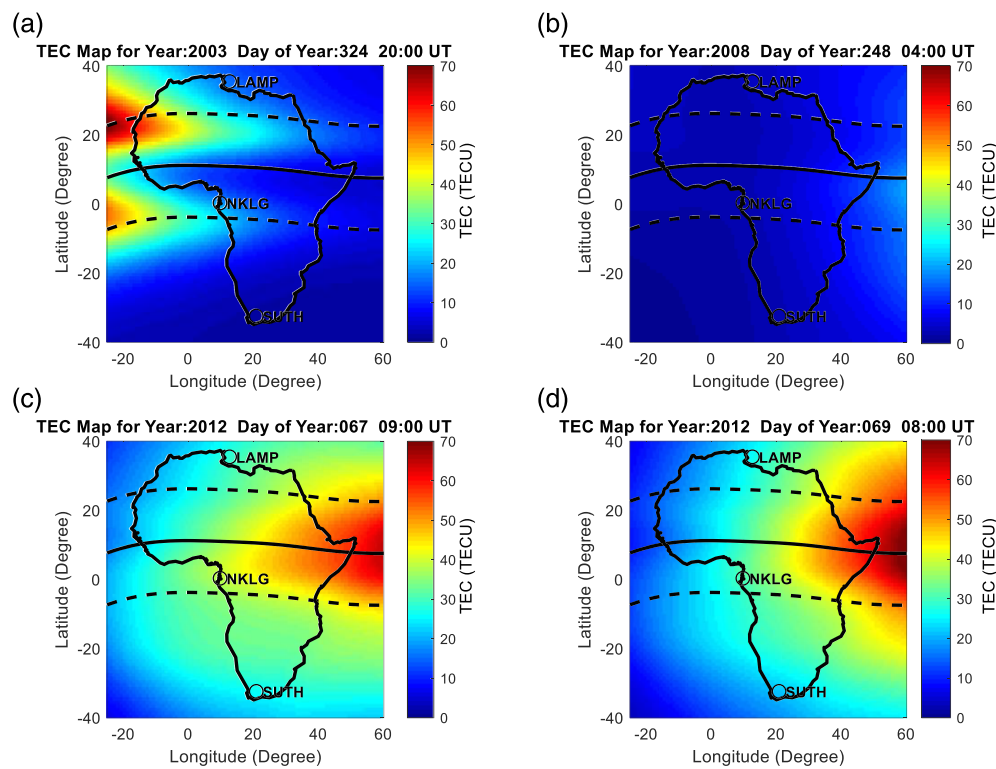


Figure 8. Spatial maps of TEC over the African region (constructed from the AfriTEC model), during the peak periods of the storms of (a) 20 November 2003, (b) 4 September 2008, (c) 7 March 2012, and (d) 9 March 2012.

derivatives. The values obtained for the network which includes the derivatives are respectively 5.0 TECU (percentage error = 30.4%), 7.5 TECU (percentage error = 22.0%), and 5.5 TECU (percentage error = 30.3%) for the LAMP, NKLG, and SUTH test data sets. For the network which does not include the derivatives, the corresponding values are 5.3 TECU (percentage error = 32.5%), 8.5 TECU (percentage error = 25.1%), and 5.8 TECU (percentage error = 32.3%). The results therefore show percentage improvements of 5.7%, 11.8%, and 5.2% respectively for the LAMP, NKLG, and SUTH stations.

Figure 8 contains sample illustrations of spatial maps of TEC over the African region, obtained from the neural network model developed in this work. Figures 8a and 8b respectively represent spatial maps of TEC over the African region, during the peaks of the storms illustrated in Figures 4 and 5. Figures 8c and 8d respectively represent the maps during the peaks of the two successive storms illustrated in Figure 6. It can be observed that the TEC values simulated in the spatial maps of Figures 8a–8d are in agreement with the corresponding values simulated in the diurnal profiles of Figures 4–6 for the three stations of LAMP, NKLG, and SUTH. For example, in Figure 8c, the TEC values at LAMP, NKLG, and SUTH are about 30 TECU, 40 TECU, and 25 TECU, respectively. These same TEC values are reflected in Figure 6 for 09:00 UT on 7 March 2012.

5. Conclusion

For the first time, we have developed a storm-time TEC model over the African sector taking into account data from 2000 to 2018 from GPS observations. Previous modeling efforts were restricted by lack of observations (Habarulema, 2010; Habyarimana et al., 2020; Matamba & Habarulema, 2018; Okoh et al., 2016) especially in the Northern Hemispheric part of the African continent and ocean areas. To address this specific issue, we made use of the TEC derived from radio occultation (COSMIC) data, scaled it to GPS TEC based on the neural network approach which led to improved coverage. The model performs better over midlatitude compared to low- and equatorial-latitude regions, a result that is consistent with other related literature (Hunt et al., 2000; Okoh et al., 2018; Uwamahoro et al., 2019) due to the complex ionospheric structure in

low latitudes related (but not limited) to steep electron density gradients, prereversal enhancements, and the presence of equatorial ionization anomaly. It was however very interesting that the accuracy of the developed model was comparable to single station modeling efforts at similar latitudes. Usually, single station models perform better than regional models because they are easier to constrain. For example, the obtained RMSE of 5.8 TECU (percentage error = 25.7%) is statistically similar to 5.7 TEC reported by Habyarimana et al. (2020) for a single station over a low latitude location (0.6°S, 30.74°E, 10.22°S magnetic). We found that inclusion of the history of geomagnetic storm indicators ($\frac{dK_p}{dt}$ and $\frac{dDst}{dt}$) improved TEC modeling by about 5% and 12% in middle- and low/equatorial-latitude regions, respectively.

Data Availability Statement

Data used in this work were obtained from the COSMIC Data Analysis and Archive Centre (<http://cosmic-io.cosmic.ucar.edu/cdaac/index.html>), the African Geodetic Reference Frame (<http://afrefdata.org>), the South African network of continuously operating GNSS base stations (<http://www.trignet.co.za>), the University of California, San Diego, SOPAC, and CSRC GARNER GPS Archive (<ftp://garner.ucsd.edu>), the National Aeronautics and Space Administration's CDDIS Archive of GNSS products (<ftp://cddis.gsfc.nasa.gov>), the Global Data Center of the International GNSS Service (<ftp://igs.ensg.ign.fr>), the UNAVCO Archive of GNSS Data (<ftp://data-out.unavco.org>), the Geodetic Data Archiving Facility (<ftp://geodaf.mt.asi.it>), the WDC-SILSO Royal Observatory of Belgium-Brussels (website: <http://www.sidc.be/silso/data-files>), the National Oceanic and Atmospheric Administration (ftp://ftp.ngdc.noaa.gov/STP/space-weather/solar-data/solar-features/solar-radio/noontime-flux/penticton/penticton_observed/listings/), NASA's OMNIWeb (<https://omniweb.sci.gsfc.nasa.gov/form/dx1.html>), and the Center for Orbit Determination in Europe (<ftp://ftp.aiub.unibe.ch/CODE/>).

Appendix A

MATLAB function: Implementation of the neural network developed.

```
function Y = net48D(X)
xoffset_in = [-0.999979192959082; -0.999999422024692; -1; -1; -25; -40; 64.6; -422; 0; -171; -4.3];
gain_in = [1.00001502754206; 1.00000751371875; 1; 1; 0.0235294117647059; 0.025; 0.0091743119266055;
0.00400801603206413; 0.22222222222222; 0.00847457627118644; 0.20833333333333];
ymin_in = -1;
ymin_out = -1;
gain_out = 0.0109268990725221;
xoffset_out = 0.04;
% Bias vectors and layer weight matrices
b1 = [3.1358414186076557506; -4.2399670618677944844; -1.4569690337791809664; -0.11291740966235
599974; -1.4872737357082670417; 3.4742588236283125092; 27.686167828396932578; -0.383358696235430
50722; 2.6993549110794243795; -0.019238122821175287352; -1.9216356720977321171; 0.9103180112183
2978119; -0.23693532015941815017; -2.3469756209442338424; -0.63988937615382013302; 0.4536785491
157435124; -8.095193853551030827; 2.8065931909340990913; 1.5625042989678754601; 0.11015654205427
845291; -5.2375401651321986662; 0.39817557520720447961; 1.6933003133080541946; -6.69566963412314
65297; -0.51117424040604175772; 0.65511847484186658264; 3.3679586970328796447; 1.59849867534772
99359; -0.4395422683065199343; -4.8696392509799668602; -1.1077914040050609312; 0.73155317208215
386859; -0.27200896018577408464; 0.3426264702052929656; 1.4721374324125038324; -2.9235574297334
04156; 1.3728504319181149551; -0.18582934625396191342; 2.3626299187604882235; 0.9298123337763344
3205; -0.42896107248419618196; -2.1142972724677830954; 1.0294898914450669736; 2.520438609855274
2368; 13.0242011722011366; -3.6000594710381612629; -12.395203407508301297; -3.6359349139339958
157];
b2 = -2.3828887136919258971;
```


981655812789; -0.0026332677999308037875; 2.1208905494254093327; 0.12427681918733946009; 0.17129809574093576852; 0.041765939421364965678; -0.13663806894700014638; -0.060287486277732012241; 1.0390933984658492495; -0.11613307417936132027; -1.9322245374078701463; -0.20679606994005048093; 0.2696642568681195673; 2.4608550787618255207; 0.69993510024699800987; 0.2297715576136677145; -0.083848052874947787139; -0.47570680011068799953; 0.2166308653163222242; -0.68444634172613172396; 2.5043914083645972823; -0.23953592304712542638; -0.66108363208418374768; -0.30276800817569360369; 6.3916891029149693892; -1.0035278205287783138; 1.5055639838168521916; -0.79464510169157509534; -1.1998147902566760337; 0.71754288111609221268; -0.32999057446060792165; 0.15100259096046375618; -0.98707801229819169819; -0.0006882578488914394086; 0.062997267414174148992; 0.6417082224003066715; -0.11552913474582678088; 0.098017596682965696386; 0.074284443447092743384; 0.31037564292355535045; -0.088088188857000773724; 1.2035441484268947221; -1.3120815456805230426; -0.20023545222950725475; -0.088434210053075751334; -0.02451213780986553209; 0.030898314422983814281; 1.0537060262392612398; -0.23065940709576879253; 2.2108560569529012163; 0.078945296566799910698; -0.92389400716187963791; -0.029835691302505209371; -0.0019341818376012826983; -0.21964610317709395981; 0.11198777619976112152; -0.072192453447961074664; -2.9803905862522603876; -0.006126187998587339506 -0.1125255004033695605; -0.028997710600355858235; 0.052800118162520233434; 0.026658943061259730845; -0.63615361598880215688; -1.9832827954997522824; -0.11844585701190994687; -0.135409370865050774993; 0.021839252711903102411; 0.16491820097073400797; 0.29970670852559416764; -0.13003624098490917937; 0.21840025939815094214; 0.16347471391510828842; -0.2452478834049835188; 15.394612470284648964; 0.31175380974270222589; -0.86241592879754491729; -0.43513348699506598782; -1.4881666041319465688; -10.960514434588731092; -14.644959334541397311; 0.4797394058136377204; -1.3735987926889710042; -2.3950679749939740582; 0.99928280639857569589; 1.2463602859272593371 0.74313074448345017853; -0.45025895428936635323; -0.043997600417459849231; -0.15021037475797247018; 0.2038970822977751729; 2.7985799380729234898; -1.4602288380874934859; -1.5482520201615712629; 1.0112167189832155234; 0.94996893002571680675; -2.6271711747596708797; -17.238092507069300297; -0.032524485319523399607; 0.35449513416156119838; 0.10848811544428110798; 0.31403433653900836298; 0.43310079768207837558; -8.9137594186949620223; -1.2569273608457922631; 2.8140579988249854182; 0.66187761125346533664; 1.238260136352266505; 0.72290827501071608374; -0.45129018566696982306; -0.054004868985043009977; -0.17713240670017241229; 0.24708819752150257276; 2.8919609953901024291; -1.5189989924621103423; -1.4603490022609124654; 0.99721528661706615448; 0.91037511765160550326];
LW2 = [-0.02427298385015888918; -2.6663549522823983828; -0.74488281625570751387; 0.87538883069055095643; 1.1795468310940255829; -0.4813746622060355862; -0.045986977559083333511; -15.353653477012272788; 0.30476229875610505449; -2.7553377518333741492; -1.249729610772658539; -13.522514007872150188; -0.3294000022280277884; -1.1914624406621285857; -24.892685458065738402; 2.7233699535032735994; -1.8764542825633179213; 0.17028864663220730225; 1.041132354265231541; 1.3934589417487710516; 0.042195387557977311055; -0.087507518424454075467; -1.691101277737376396; 2.2529541116097733244; 1.1037713148669716645; 1.4686772748469321126; -0.093434714700805041043; -5.9620777163285740841; 6.3716709709231773573; 2.5932084799978607492; -0.19654697823698144554; 5.2238104084674716887; 0.67007142581273670956; -22.267177716812074806; 0.098819418449648283032; 1.1784303752052340819; 11.403696532389655971; -8.6814535685974814072; 0.25631593150405973525; -0.0497220710399917179; 2.5893893237532243923; 0.30110142756542085385; -11.849573759487508795; 1.234221615357030899; 0.037152116423089416586; 6.1226447702881046098; 0.11108086588780853587; -6.1567300475479633803];

X = X';

N = size (X, 2);

% Normalization

yy = bsxfun (@minus, X, x offset_in);

yy = bsxfun (@times, yy, gain_in);

Xp1 = bsxfun(@plus, yy, y min_in);

% Transfer Function 1

```
n1 = repmat (b1, 1, N) + LW1 * Xp1;
a1 = 2./(1 + exp(-2 * n1)) - 1;
% Transfer Function 2
n2 = repmat (b2, 1, N) + LW2 * a1;
a2 = 2./ (1 + exp(-2*n2)) - 1;
% Denormalization
xx2 = bsxfun(@minus,a2,ymin_out);
xx2 = bsxfun(@rdivide, xx2, gain_out);
Y = bsxfun(@plus, xx2, xoffset_out);
Y = Y';
end.
```

Acknowledgments

This research was funded and supported by the South African National Space Agency (SANSA) Space Science and the Centre for Atmospheric Research (CAR) of the National Space Research and Development Agency, Nigeria. We appreciate management and staff of the Space Weather Center, SANSA, for the various supports they gave.

References

- Adebesin, B. O. (2008). *F2* region response to the magnetic storm of January 10, 1976 at American sector. *The African Review of Physics*, 2, 136–142.
- Adebisi, S. J., Adimula, I. A., Oladipo, O. A., Joshua, B. W., Adebesin, B. O., & Ikubanni, S. O. (2014). Ionospheric response to magnetic activity at low and mid-latitude stations. *Acta Geophysica*, 62(4), 973–989.
- Adekoya, B. J., Chukwuma, V. U., Bakare, N. O., & David, T. W. (2012). Effects of geomagnetic storm on middle latitude ionospheric *F2* during storm of 2–6 April 2004. *Indian Journal of Radio & Space Physics*, 41(6), 606–616.
- Akala, A. O., Somoye, E. O., Adewale, A. O., Ojutalayo, E. W., Karia, S. P., Idolor, R. O., et al. (2015). Comparison of GPSTEC observations over Addis Ababa with IRI-2012 model predictions during 2010–2013. *Advances in Space Research*, 56(8), 1686–1698. <https://doi.org/10.1016/j.asr.2015.07.017>
- Appleton, E. (1950). Magnetic and ionospheric storms. *Archiv für Meteorologie, Geophysik und Bioklimatologie, Serie A*, 3(1–2), 113–119. <https://doi.org/10.1007/BF02247526>
- Bayes, T. (1763). An essay towards solving a problem in the doctrine of chances. *Philosophical Transactions*, 53, 370–418. <https://doi.org/10.1098/rstl.1763.0053>
- Burden, F., & Winkler, D. (2008). Bayesian regularization of neural networks. In D. J. Livingstone (Ed.), *Artificial neural networks. Methods in molecular biology* (Vol. 458, pp. 23–42). New York City: Humana Press. https://doi.org/10.1007/978-1-60327-101-1_3
- Catherine, J. K., Maheshwari, D. U., Gahalaut, V. K., Roy, P. N. S., Khan, P. K., & Puvirasan, N. (2017). Ionospheric disturbances triggered by the 25 April, 2015 M7.8 Gorkha earthquake, Nepal: Constraints from GPS TEC measurements. *Journal of Asian Earth Sciences*, 133, 80–88.
- Chen-Joe, F. (2008). Constellation deployment for the FORMOSAT-3/COSMIC Mission. *IEEE Transactions on Geoscience and Remote Sensing*, 46(11), 3367–3379.
- Dubazane, M. B., & Habarulema, J. B. (2018). An empirical model of vertical plasma drift over the African sector. *Space Weather*, 16, 619–635. <https://doi.org/10.1029/2018SW001820>
- Findlay, J. A., Dyson, P. L., Brace, L. H., Zmuda, A. J., & Radford, W. E. (1969). Ionospheric and magnetic observations at 1000 kilometers during the geomagnetic storm and aurora of May 25–26, 1967. *Journal of Geophysical Research*, 74(14), 3705–3712. <https://doi.org/10.1029/JA074i014p03705>
- Guyer, S., & Can, Z. (2013). *Solar flare effects on the ionosphere* (pp. 729–733). Istanbul: 2013 6th International Conference on Recent Advances in Space Technologies (RAST).
- Habarulema, J. B. (2010). *A contribution to TEC modelling over Southern Africa using GPS data*. Grahamstown, South Africa: PhD Thesis, Rhodes University.
- Habarulema, J. B., McKinnell, L. A., & Cilliers, P. J. (2007). Prediction of Global Positioning System total electron content using neural networks over South Africa. *Journal of Atmospheric and Solar - Terrestrial Physics*, 69(15), 1842–1850. <https://doi.org/10.1016/j.jastp.2007.09.002>
- Habyarimana, V., Habarulema, J. B., & Mungufeni, P. (2020). On the possible contribution of ionospheric vertical drifts to TEC modelling in low latitudes. *Advances in Space Research*, 65(10), 2391–2404. <https://doi.org/10.1016/j.asr.2020.02.005>
- Hunt, S. M., Close, S., Coster, A. J., Stevens, E., Schuett, L. M., & Vardaro, A. (2000). Equatorial atmospheric and ionospheric modeling at Kwajalein missile range. *Lincoln Laboratory Journal*, 12(1), 45–64.
- Joshua, B. W., Adeniyi, J. O., Oladipo, O. A., Doherty, P. H., Adimula, I. A., Olawepo, A. O., & Adebisi, S. J. (2018). Simultaneous response of NmF2 and GPS-TEC to storm events at Ilorin. *Advances in Space Research*, 61(12), 2904–2913.
- Laplace, P. S. (1812). *Theorie analytique des probabilités*. Paris: Ve. Courcier.
- MacKay, D. (1992). Bayesian interpolation. *Neural Computation*, 4(3), 415–447. <https://doi.org/10.1162/neco.1992.4.3.415>
- Matamba, T. M., & Habarulema, J. B. (2018). Ionospheric responses to CME- and CIR-driven geomagnetic storms along 30°E–40°E over the African sector from 2001 to 2015. *Space Weather*, 16, 538–556. <https://doi.org/10.1029/2017SW001754>
- Matamba, T. M., Habarulema, J. B., & McKinnell, L.-A. (2015). Statistical analysis of the ionospheric response during geomagnetic storm conditions over South Africa using ionosonde and GPS data. *Space Weather*, 13, 536–547. <https://doi.org/10.1002/2015SW001218>
- Mathworks (2020). Boxplot, <https://www.mathworks.com/help/stats/boxplot.html>
- Mikhailov, A., & Schlegel, K. (1998). Physical mechanism of strong negative storm effects in the daytime ionospheric *F2* region observed with EISCAT. *Annales Geophysicae*, 16(5), 602–608.
- Namgaladze, A. A., Förster, M., & Yurik, R. Y. (2000). Analysis of the positive ionospheric response to a moderate geomagnetic storm using a global numerical model. *Annales Geophysicae*, 18(4), 461–477. <https://doi.org/10.1007/s00585-000-0461-8>

- Nava, B., Rodríguez-Zuluaga, J., Alazo-Cuarteras, K., Kashcheyev, A., Migoya-Orué, Y., Radicella, S. M., et al. (2016). Middle-and low-latitude ionosphere response to 2015 St. Patrick's Day geomagnetic storm. *Journal of Geophysical Research: Space Physics*, 121, 3421–3438. <https://doi.org/10.1002/2015JA022299>
- Ngwira, C. M., McKinnell, L. A., Cilliers, P. J., & Coster, A. J. (2012). Ionospheric observations during the geomagnetic storm events on 24–27 July 2004: Long-duration positive storm effects. *Journal of Geophysical Research*, 117, 1–13. <https://doi.org/10.1029/2011JA016990>
- Okoh, D., Onwuneme, S., Seemala, G., Jin, S., Rabiu, B., Nava, B., & Uwamahoro, J. (2018). Assessment of the NeQuick-2 and IRI-Plas 2017 models using global and long-term GNSS measurements. *Journal of Atmospheric and Solar - Terrestrial Physics*, 170, 1–10. <https://doi.org/10.1016/j.jastp.2018.02.006>
- Okoh, D., Owolabi, O., Ekechukwu, C., Folarin, O., Arhiwo, G., Agbo, J., et al. (2016). A regional GNSS-VTEC model over Nigeria using neural networks: A novel approach. *Geodesy & Geodynamics*, 7(1), 19–31. <https://doi.org/10.1016/j.geog.2016.03.003>
- Okoh, D., Seemala, G., Rabiu, B., Habarulema, J. B., Jin, S., Shiokawa, K., et al. (2019). A neural network-based ionospheric model over Africa from Constellation Observing System for Meteorology, Ionosphere, and Climate and Ground Global Positioning System observations. *Journal of Geophysical Research: Space Physics*, 124, 10,512–10,532. <https://doi.org/10.1029/2019JA027065>
- Olawepo, A. O., & Adeniyi, J. O. (2012). Ionosphere's F2-layer response to 2006 geomagnetic storm at Ilorin, Nigeria. *The African Review of Physics*, 7(277), 0031.
- Olwendo, O. J., Baki, P., Mito, C., & Doherty, P. (2012). Characterization of ionospheric GPS total electron content (GPS-TEC) in low latitude zone over the Kenyan region during a very low solar activity phase. *Journal of Atmospheric and Solar - Terrestrial Physics*, 84–85, 52–61. <https://doi.org/10.1016/j.jastp.2012.06.003>
- Panda, S. K., Gedam, S. S., & Rajaram, G. (2015). Study of Ionospheric TEC from GPS observations and comparisons with IRI and SPIM model predictions in the low latitude anomaly Indian subcontinental region. *Advances in Space Research*, 55(8), 1948–1964.
- Pedatella, N. M., Lei, J., Larson, K. M., & Forbes, J. M. (2009). Observations of the ionospheric response to the 15 December 2006 geomagnetic storm: Long-duration positive storm effect. *Journal of Geophysical Research*, 114, A12313. <https://doi.org/10.1029/2009JA014568>
- Rabiu, A. B., Adewale, A. O., Abdulrahim, R. B., & Oyeyemi, E. O. (2014). TEC derived from some GPS stations in Nigeria and comparison with the IRI and Ne quick models. *Advances in Space Research*, 53(9), 1290–1303. <https://doi.org/10.1016/j.asr.2014.02.009>
- Rabiu, A. B., Mamukuyomi, A. I., & Joshua, E. O. (2007). Variability of equatorial ionosphere inferred from geomagnetic field measurements. *Bulletin of the Astronomical Society of India*, 35, 607–618.
- Rama Rao, P. R., Niranjan, K., Prasad, D., Krishna, S. G., & Uma, G. (2006). On the validity of the ionospheric pierce point IPP altitude of 350 km in the Indian equatorial and low-latitude sector. *Annales Geophysicae*, 24(8), 2159–2168. <https://doi.org/10.5194/angeo-24-2159-2006>
- Sato, T. (1957). Disturbances in the ionospheric F2 region associated with geomagnetic storms. III. Auroral latitudes. *Journal of Geomagnetism and Geoelectricity*, 9(2), 94–106.
- Scherliess, L., & Fejer, B. G. (1999). Radar and satellite global equatorial F region vertical drift model. *Journal of Geophysical Research*, 104(A4), 6829–6842. <https://doi.org/10.1029/1999JA900025>
- Seemala, G. K., & Valladares, C. E. (2011). Statistics of total electron content depletions observed over the South American continent for the year 2008. *Radio Science*, 46, RS5019. <https://doi.org/10.1029/2011RS004722>
- Strickland, D. J., Daniell, R. E., & Craven, J. D. (2001). Negative ionospheric storm coincident with DE 1-observed thermospheric disturbance on October 14, 1981. *Journal of Geophysical Research*, 106(A10), 21,049–21,062.
- Syndergaard, S., Schreiner, W. S., Rocken, C., Hunt, D. C., & Dymond, K. F. (2006). Preparing for cosmic: Inversion and analysis of ionospheric data products. In U. Foelsche, G. Kirchengast, & A. K. Steiner (Eds.), *Atmosphere and climate: Studies by occultation methods* (pp. 137–146). New York: Springer.
- Uwamahoro, J. C., Giday, N. M., Habarulema, J. B., Katamzi-Joseph, Z. T., & Seemala, G. K. (2018). Reconstruction of storm-time total electron content using ionospheric tomography and artificial neural networks: A comparative study over the African region. *Radio Science*, 53, 1328–1345. <https://doi.org/10.1029/2017RS006499>
- Uwamahoro, J. C., & Habarulema, J. B. (2015). Modelling total electron content during geomagnetic storm conditions using empirical orthogonal functions and neural networks. *Journal of Geophysical Research: Space Physics*, 120, 11,000–11,012. <https://doi.org/10.1002/2015JA021961>
- Uwamahoro, J. C., Habarulema, J. B., & Buresova, D. (2019). Highlights about the performances of storm-time TEC modeling techniques for low/equatorial and mid-latitude locations. *Advances in Space Research*, 63(10), 3102–3118. <https://doi.org/10.1016/j.asr.2019.01.027>
- Yamazaki, Y., & Kosch, M. J. (2015). The equatorial electrojet during geomagnetic storms and substorms. *Journal of Geophysical Research: Space Physics*, 120, 2276–2287. <https://doi.org/10.1002/2014JA020773>
- Yeh, K. C., Ma, S. Y., Lin, K. H., & Conkright, R. O. (1994). Global ionospheric effects of the October 1989 geomagnetic storm. *Journal of Geophysical Research*, 99(A4), 6201–6218.
- Yue, X., Wang, W., Lei, J., Burns, A., Zhang, Y., Wan, W., et al. (2016). Long-lasting negative ionospheric storm effects in low and middle latitudes during the recovery phase of the 17 March 2013 geomagnetic storm. *Journal of Geophysical Research: Space Physics*, 121, 9234–9249. <https://doi.org/10.1002/2016JA022984>